# SPASM: Segmentation of Sparse and Arbitrarily Oriented Cardiac MRI Data Using a 3D-ASM

Hans C. van Assen[1], Mikhail G. Danilouchkine[1], Alejandro F. Frangi[2], Sebastián Ordás[2], Jos J.M. Westenberg[1], Johan H.C. Reiber[1], and Boudewijn P.F. Lelieveldt[1]

[1] Div. of Image Processing, Dep. of Radiology, Leiden University Medical Center, PO BOX 9600, 2300 RC, Leiden, Netherlands
b.p.f.lelieveldt@lumc.nl
http://www.lkeb.nl
[2] Computational Imaging Laboratory, Department of Technology, Universitat Pompeu Fabra, Barcelona, Spain
http://www.cilab.upf.edu

**Abstract.** In this paper, a new technique (SPASM) based on a 3D-ASM is presented for automatic segmentation of cardiac MRI image data sets consisting of multiple planes with different orientations, and with large undersampled regions. SPASM was applied to sparsely sampled and radially oriented cardiac LV image data.

Performance of SPASM has been compared to results from other methods reported in literature. The accuracy of SPASM is comparable to these other methods, but SPASM uses considerably less image data.

## 1 Introduction

Nowadays, cardiac MRI and CT are increasingly used for cardiac functional analysis in daily clinical practice. Both modalities yield dynamic 3D image data sets. With CT, images are acquired in an axial orientation and for cardiac analysis, usually short-axis (SA) views are reconstructed from the axial image data. With MRI, images can be acquired in any spatial orientation. Commonly used orientations are short-axis and long-axis (LA) views (2-chamber and 4-chamber), and radial stacks. The SA acquisitions consist of a full stack of typically 8 to 12 (parallel) slices covering the heart from apex to base. However, there is an ongoing debate on potential improvement of functional measurements by using LA views or radially scanned long-axis (RAD) image slices, since they appear to give better volume quantification due to better definition of the apex and base [1].

For quantitative analysis of cardiac function, typically a cardiologist or radiologist manually segments the images. After segmentation, measurements of global and regional functional parameters can be performed, such as wall thickening or wall thinning, LV volume and Ejection Fraction (EF). Due to the increasing amount of data, the amount of work for manually delineating the image data has become prohibitively large, and automated segmentation is highly desired.

A.F. Frangi et al. (Eds.): FIMH 2005, LNCS 3504, pp. 33–43, 2005.

Recent work has shown that integration of prior knowledge into medical image segmentation methods is essential for robust performance. Many recent methods utilize a statistical shape model, and the seminal work of Cootes [2,3] on 2D Active Shape Models (ASMs)- and Active Appearance Models (AAMs) has inspired the development of 3D ASMs [4,5], 3D AAMs [6], 3D Spherical Harmonics (SPHARM) [7], 3D Statistical Deformation Models (SDMs) [8,9,10, 11] and 3D medial representations (m-reps) [12]. However, all these statistical models are only applicable to densely sampled 3D volume data, because the modeling mechanism is either based on a dense volumetric registration [6,8,9, 10,11] or the matching mechanism is based on a dense set of updates along the model surface [4,5,12]. Therefore they typically assume a near isotropic resolution and parallel image planes. The main goal of this work is to avoid the need for these requirements on data sampling by developing a 3D active shape model that:

- is applicable to sparsely sampled data sets without making assumptions about voxel isotropy or parallel slices.
- is extensible to other modalities without retraining the shape model

To accomplish this, we present a 3D-Active Shape Model (3D-ASM) of the cardiac left ventricle (LV). The underlying statistical shape model was based on a 3D atlas that was constructed using non-rigid registration [9,13]. Matching of the model to sparse, arbitrarily oriented image data is accomplished through a deformable mesh that enables propagation of image updates over the model surface. Independence of a trained gray level model is achieved through a Takagi-Sugeno Fuzzy Inference System (TSFIS) [14] for determining iterative model updates based on *relative* intensity differences [4].

## 2 Background

Active Shape Models were introduced by Cootes et al. [2,15] and consist of a statistical shape model (often referred to as Point Distribution Model (PDM)) and a matching algorithm. The PDM is trained from a population of typical examples of the target shape, and models shape variability as a linear combination of a mean shape, i.e. a mean set of (pseudo-)landmarks, and a number of eigenvariations. For an elaborate introduction to ASMs, the reader is referred to [2,15,16].

### 2.1 Atlas Construction

A critical issue to achieve extension of PDMs to three and more dimensions is point correspondence: the landmarks have to be placed in a consistent way over a large database of training shapes, otherwise an incorrect parameterization of the object class would result. The methodology employed to automatically achieve this point correspondence of the heart was described in detail in [9]. The general layout of the method is to align all the images of the training set to a mean atlas (Fig. 1). The transformations are a concatenation of a global rigid registration

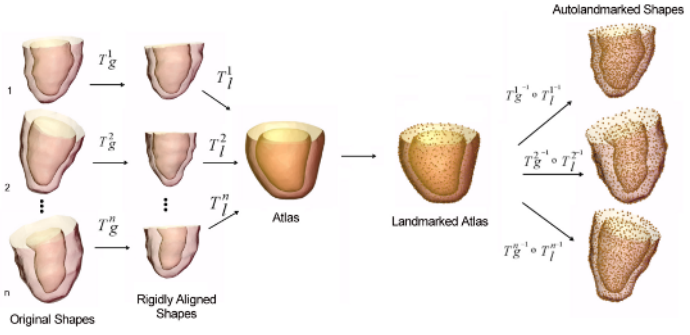


**Fig. 1.** Atlas construction, a set of final global ($T_g$) and local ($T_l$) transformations can take any sample shape of the training set, to the atlas coordinate system. On the left, there is landmark propagation. Once the final global and local transformations are obtained, they are inverted and used to propagate any number of arbitrarily sampled landmarks on the atlas, to the coordinate system of the original samples

with nine degrees of freedom (translation, rotation, and anisotropic scaling) and a local transformation using non-rigid registration. After registration of all samples to the mean shape, the transformations are inverted to propagate a topologically fixed point set on the atlas surface to the coordinate system of each training shape. While it is still necessary to manually segment each training image, this technique reliefs from manual landmark definition. The method can easily be set to build either 1- or 2-chamber models; in this work we have used a 1-chamber model. To build the statistical shape model, the auto-landmarked shapes are aligned using Procrustes alignment [17]. Principal Component Analysis (PCA) can then be performed on the remaining differences, which are solely shape related.

### 2.2 Matching Algorithm

The model described above was extended with a matching algorithm to apply it to image segmentation. A key design criterion behind this matching approach was applicability to data acquired with arbitrary image slice orientations, from different modalities (MR and CT), and even to sparsely sampled data with arbitrary image slice orientations. This implies that:

- only 2D image data may be used for updating the 3D model, to ensure applicability to arbitrarily oriented sparse data
- generation of update points is performed based on relative intensity difference to remove the dependence on training-based gray-level models.

To accomplish this, the landmark points are embedded in a surface triangular mesh. During the matching, this mesh is intersected by the image planes, generating 2D contours spanned by the intersections of the mesh triangles. To remove dependencies on image orientation or limited resolution, model update information is represented by 2D point-displacement vectors. The 2D update

vectors located at the intersections of the mesh with the image slices are first propagated to the nodes of the mesh, and projected onto the local surface normals. Scaling, rotation, and translation differences between the current state of the model and the point cloud representing the candidate updates are eliminated by alignment. The current model state is aligned with the candidate model state (i.e., current model state with nodes displaced by the update vectors inferred from image information) using the Iterative Closest Point algorithm [18]. Successively, the parameter vector $\boldsymbol{b}$ controlling model deformation is calculated. An adjustment to $\boldsymbol{b}$ with respect to the previous iteration is computed, using both the candidate model state, $\hat{\boldsymbol{x}}_{n+1}$, and the current model state, $\boldsymbol{x}_n$

$$\hat{\boldsymbol{b}}_{n+1} = \boldsymbol{b}_n + \Delta\boldsymbol{b} = \boldsymbol{b}_n + \Phi^T(\hat{\boldsymbol{x}}_{n+1} - \boldsymbol{x}_n) \tag{1}$$

with $\boldsymbol{x_n}$ representing the aligned current state of the mesh, and $\boldsymbol{b_n}$ representing the parameter vector describing the current shape of the model within the statistical bounds. The vector $\hat{\boldsymbol{x}}_{\boldsymbol{n+1}}$ is the proposed model shape for the next iteration, and $\hat{\boldsymbol{b}}_{\boldsymbol{n+1}}$ its shape parameter vector before statistical constraints have been applied.

### 2.3 Update Propagation to Undersampled Surface Regions

In densely sampled data, a 3D data volume can be reconstructed that enables generation of a 3D update in each model landmark. However, in sparsely sampled data containing large undersampled regions, a (dense) 3D data volume cannot be reconstructed: interpolation between sparse image slices with different orientations (e.g., a radial stack of cardiac LA views) is non-trivial, if at all possible. In void locations, no information can be extracted from the image data to contribute to a new model instance. However, for the calculation of new model parameters, updates for the complete landmark set are required: setting updates of zero displacement would fixate the nodes to their current position, thus preventing proper model deformation.

Paulsen et al. [19] applied Gaussian smoothing of a mesh surface in combination with a Markov Random Field for restoration of point correspondences for an ear canal ASM. During the deformation of a mesh to presegmented shapes of ear canals and projection of the mesh nodes on the target shape, swapping of mesh vertices could occur. Instead of the training stage, we apply a similar method to the matching stage of SPASM. To overcome large void areas without update information, we propose a node propagation mechanism that distributes the updates from non-void update locations towards the void regions (see Fig. 2(a)). This mesh update propagation is weighted with the geodesic distance to the origin of the update using a Gaussian kernel (see Fig 2(b)):

$$w(x) = e^{-\frac{\|x-\omega\|^2}{2\sigma^2}} \tag{2}$$

where $w(x)$ is the weight at the location of the receiving node in the mesh $x$, $\omega$ is the source node, $\|x - \omega\|$ is the geodesic distance to the origin of the update, $\sigma$ is the width of the kernel. Therefore, if multiple paths exist from source node to receiving node, only the shortest path is used. Thus, a receiving node accepts

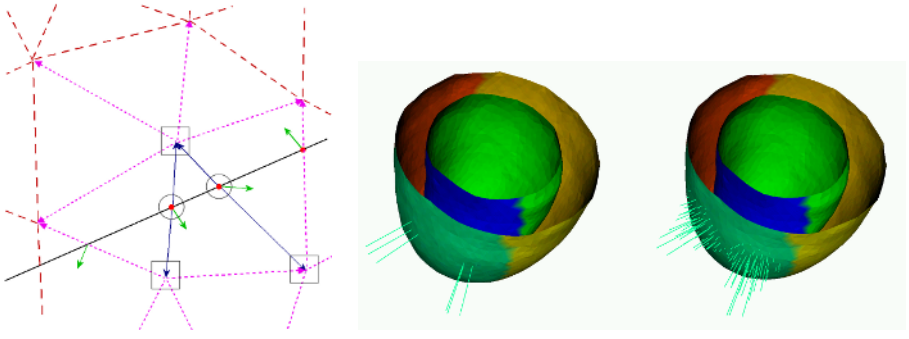

(a) (b)

**Fig. 2.** (a) Propagation of single model updates at the intersection with an image plane (solid line). Propagation from the update sources surrounded with a circle is illustrated here. From a source, an update vector originates (short arrow). Updates are first propagated (longer solid arrows) to the nearest nodes in the mesh (marked with squares). Updates are further propagated to adjacent nodes weighted with a Gaussian kernel. Secondary updates (dotted lines) and tertiary updates (dashed lines) are also shown. (b) Gaussian propagation with $\sigma = 4mm$ (right) of two model updates (left)

propagated updates from any source only once. To avoid propagation updates over the entire surface, propagation is stopped when the geodesic distance exceeds a fixed threshold ($\chi \equiv 3\sigma$). After all propagations stopped, a pruning of all node updates is performed. Each node has a list of weighted contributions from source nodes, and a list of weights that were used to calculate each contribution. A total update per node is computed by summing over all contributions and normalizing with the sum of the weights.

### 2.4 Edge Detection Using Fuzzy Inference

The mesh structure combined with the update propagation enables applications to sparsely and arbitrarily oriented data. To apply the model to different modalities without retraining, the matching algorithm should not employ any trained intensity model to generate the updates. Instead, we have developed an update mechanism based on a Takagi-Sugeno Fuzzy Inference System (TSFIS) [14], which uses Fuzzy C-Means clustering (FCM) on the gray values of a 3D volume patch surrounding the current instance of the model (see Fig. 3(c)). This approach has been described in detail in [4], and can be summarized as follows:

1. *Input*
   *For each intersection point between the mesh and each of the 2D images, an image patch, centered in this point, is considered. Patch size was selected such that multiple tissues were included in the patch.*

2. *Sectorization*
   *To overcome possible inhomogeneities in the gray value distributions due to surface coil effects, the ventricle shape is divided in multiple sectors. Patches are pooled following this sectorization, enabling application of different rule sets for different anatomical sectors the LV.*
3. *Fuzzification*
   *To locate tissue transitions, gray values are classified per sector based on relative intensity differences between blood, myocardium and air using standard Fuzzy C-Means (FCM) [20] clustering. In this work, the classes in the FCM are bright, dark, and medium bright, representing blood pool, air and myocardium respectively.*
4. *Inference of model updates*
   *For each pixel, three fuzzy membership degrees (FMDs) result from fuzzy clustering, above. Based on the FMDs, a mesh update is inferred as follows:*
   (a) *defuzzification for each pixel*
   *if (gray value is bright) then pixel is blood pool*
   *if (gray value is medium) then pixel is myocardium*
   *if (gray value is dark) then pixel is air*
   *However, pixels are only classified if they clearly belong to one tissue class. If a pixel does not reach a preset minimum membership degree for any tissue class (see Table 1), it is not classified and not considered for inference.*
   (b) *transition inference*
   *endocardial border: from outside to inside, find the first transition from myocardium to blood pool*
   *epicardial border:*
   a *at the septum*
   *from inside to outside, first transition from myocardium to blood pool*
   b *at the lung, anterior and posterior wall*
   *from inside to outside, first transition from myocardium to another tissue*


(a) (b) (c)

**Fig. 3.** (a) Radial cardiac image stack. (b) Radial slice acquired with the Turbo Field Echo (TFE) protocol. (c) Classified set of image patches. (A=LV blood pool, B=RV blood pool, C=myocardium, D=air, E=outside image patches)

**Table 1.** Parameters of the SPASM and their values

| **Defuzzification** [21] | | **ASM** | |
|---|---|---|---|
| Air cut-off proport. (See [4]) | -0.20 | Modes of variation | 60 |
| Blood pool mem.ship thresh. | 0.20 | Max variation per mode | $2\sigma$ |
| Myocardium mem.ship thresh. | 0.05 | **Propagation** | |
| Air mem.ship thresh. | 0.50 | Gauss. kern. width $\sigma$ (Eq. (2)) | $8mm$ |

## 3 Experimental Setup

### 3.1 Test Data and Protocol

To test the performance of the sparse data model, a group of 15 volunteers was scanned with a Philips Gyroscan NT5 (1.5T) scanner, using the Steady State Free Procession (SSFP) and the Turbo Field Echo (TFE) protocols. For all scans and protocols, the QBody coil was used. A number of acquisitions with different slice orientations were performed during breath hold in end expiration. First, SA images were acquired, yielding a stack of typically 10-12 parallel image slices. Next, a radial scan was performed comprising four LA image slices, with inter-slice angle of 45° (see Fig. 3(a)). To avoid breathing-induced slice shifts, every slice was acquired with the TFE protocol, acquiring all four slices in the same breath hold. Image slices had a $256^2$ matrix and covered a field-of-view of $300 - 400mm$, slice thickness and slice gap for the SA acquisitions were $8mm$ and $2mm$ respectively. For the RAD TFE acquisitions, the slice thickness was $8mm$. LV contours were manually drawn in all data sets. The manual contours in the radial stack were used to compensate for slice shifts in the SA volume due to differences in inspiration level. To assess inter-observer variability with respect to manual delineation, contours on all subjects were drawn by two observers.

### 3.2 Matching

Initialization of the model in the target data set was performed manually. Initial pose and scale were calculated from manual delineations on the image data from the SA acquisition. Due to the rotational symmetry of the model with respect to the long-axis and the sectorization, special attention was paid to initialize the model such that the myocardial sectors corresponded to the approximately correct anatomical location in the image data.

Parameter settings for the membership thresholds for the FIS used to define model updates at locations where the model is intersected by image planes were taken from previous work [21]. Best settings for the propagation parameters were determined in an exhaustive search on a computer cluster with 50 processors, using point-to-surface (P2S) error measures of the final state of the model with respect to manual segmentation as criterion for evaluation. The optimal settings for the parameters are listed in Table 1.

### 3.3 Quantitative Evaluation

To quantify the performance of the SPASM on the sparse radial image data, point-to-surface (P2S) error measurements were performed (see Fig. 5. Manually delineated surfaces in the SA image data were selected as gold standard. In addition, a comparison was performed between volumes of the final model states and volumes derived from the manual segmentations on the SA acquisition data.

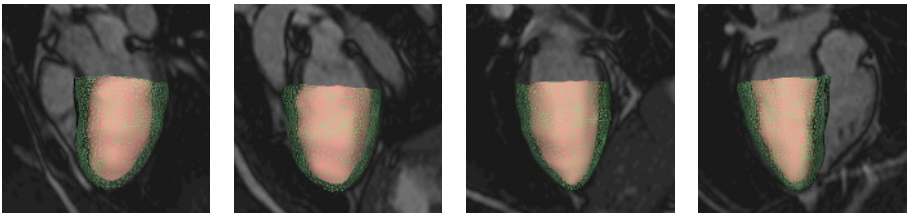

(a) (b) (c) (d)

**Fig. 4.** Final segmentation result of one of the subjects in the test population. (a-d) Result shown on slice 1 through 4, respectively

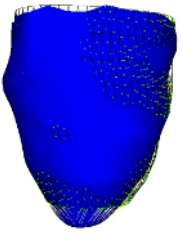

**Fig. 5.** Point-to-surface error measurement. Distances are measured from points on the automatic surface (solid) to the manually segmented surface (mesh). Note that the largest errors are made at the apical region

## 4 Results

Results from the tuning of the update propagation parameters are shown in Table 1. Results from the P2S evaluations between the final model instance and

[1] These are the best obtained results by Lötjönen et al [11] with a 4-chamber ASM based on a probabilistic atlas. Other models were built using normalized mutual information, landmark probability distribution, PCA, and ICA.

[2] Mitchell et al. compute errors of the automatic segmentation results slightly different than in this work. Mitchell et al compute (2D) distances in the image slices along lines perpendicular to the centerline between automatic and manual segmented contours. This does not guarantee shortest point-to-curve or point-to-surface distances, and may thus overestimate errors with respect to the method used in this paper and by Lötjönen et al.

**Table 2.** Point-to-surface distances measured per subject between manual and automatic surfaces in *mm*, averaged over the total population (14 subjects). Maximum distances are maximum distances per subject averaged over the total population.(all values are average ± standard deviation in *mm*)

| | Average | | Maximum | |
|---|---|---|---|---|
| | *endocard* | *epicard* | *endocard* | *epicard* |
| Inter observer | 1.27 ± 0.30 | 1.14 ± 0.29 | 4.34 ± 0.88 | 3.93 ± 0.79 |
| Lötjönen et al. (aut. ref.) [11][1] | 2.01 ± 0.31 | 2.77 ± 0.49 | n.a. | n.a. |
| Mitchell et al. [6][2] | 2.75 ± 0.86 | 2.63 ± 0.76 | n.a. | n.a. |
| Kaus et al. [5] | 2.28 ± 0.93 | 2.62 ± 0.75 | 13.82 | 12.35 |
| SPASM | 2.24 ± 0.54 | 2.83 ± 0.78 | 11.1 ± 2.54 | 15.7 ± 5.06 |

**Table 3.** Volume regression numbers. Volumes were calculated per subject (14 subjects), separately for endocardial volume and epicardial volume. Volume calculated from SA reconstruction was taken as the reference volume (ground truth)

| | Correlation coefficient (R) | |
|---|---|---|
| | *endocardium* | *epicardium* |
| Manual volume (radial image slices) | 0.74 | 0.71 |
| Automatic volume | 0.78 | 0.74 |

manual segmentations in SA views are presented in Table 2. Correlation coefficients between manual volumes from SA views and automatic volumes from the final model instance are shown in Table 3. For comparison, the correlation coefficients between manually segmented volumes from SA views and from RAD views are presented in Table 3 as well. In the results, one subject was excluded due to a mismatch for almost all the runs in the tuning process on this subject. A final segmentation result of one of the subjects is shown on all four slices in Figure 4. Matching for $N_{max} = 100$ iterations took 727 ± 134 seconds (minimal 522 seconds, maximal 915 seconds) on a 2.8 GHz Xeon computer machine running Linux Redhat 9.

## 5 Discussion and Conclusion

In this paper SPASM is presented, a new technique based on a 3D-ASM, that is able to automatically segment cardiac MRI image data sets consisting of multiple planes with different orientations, and having large undersampled regions.

Because SPASM does not include a statistical gray level model, it is potentially applicable to both MRI and CT data sets without fully retraining the intensity model. For segmentation, it does not require image slices with equal orientations as present in the training data. SPASM was applied to radially oriented cardiac LV image data, which contains undersampled regions with larger sampling density at the apex than at the base.

Performance of SPASM was evaluated against manual delineations on an SA data set of the same subjects. In the SA data set, the heart can be displaced between different slice acquisitions, due to different breath hold levels. Although this displacement is minimized by acquisition during end expiration, correction of slice positions was necessary.

The maximum errors presented in Table 2 are mainly observed at the apical regions (see Fig. 5). This is due to the closed apex in SPASM, while the manual segmentation at the apex is open.

Performance of SPASM has been compared to results from other methods reported in literature [6, 11, 5] (see Table 2). The accuracy of SPASM is comparable to these other methods. However, SPASM is the only method that can be applied to a set of arbitrarily oriented and sparsely sampled image slices: it was applied to only four image slices, whereas the other models required a stack of 8-12 parallel slices, yielding comparable accuracy. Segmentation errors of all methods are substantially larger than the inter-observer variability (see Table 2). This may be caused by too rigid statistical constraints on the allowed deformation of statistical shape models in general. Further evaluation of SPASM is ongoing with respect to the minimally required sampling density, different combinations of LA and SA image slice orientations, and the sensitivity of the final segmentation results to model initialization.

## References

1. T. N. Bloomer, S. Plein, A. Radjenovic, D. M. Higgins, T. R. Jones, J. P. Ridgway, and M. U. Sivananthan, "Cine mri using steady state free precession in the radial long axis orientation is a fast accurate method for obtaining volumetric data of the left ventricle," *Journal of Magnetic Resonance Imaging*, vol. 14, pp. 685–692, 2001.
2. T. F. Cootes, D. Cooper, C. J. Taylor, and J. Graham, "Active shape models - their training and application," *Computer Vision and Image Understanding*, vol. 61, no. 1, pp. 38–59, 1995.
3. T. F. Cootes, G. J. Edwards, and C. J. Taylor, "Active appearance models," *IEEE Transactions on Patern Analysis and Machine Intelligence*, vol. 23, no. 6, pp. 681–685, 2001.
4. H. C. van Assen, M. G. Danilouchkine, M. S. Dirksen, J. H. C. Reiber, and B. P. F. Lelieveldt, "A 3d-active shape model driven by fuzzy inference: Application to cardiac ct and mr," *submitted*.
5. M. R. Kaus, J. von Berg, J. Weese, W. Niessen, and V. Pekar, "Automated segmentation of the left ventricle in cardiac mri," *Medical Image Analysis*, vol. 8, no. 13, pp. 245–254, 2004.
6. S. C. Mitchell, J. G. Bosch, B. P. F. Lelieveldt, R. J. van der Geest, J. H. C. Reiber, and M. Sonka, "3d active appearance models: Segmentation of cardiac mr and ultrasound images," *IEEE Transactions on Medical Imaging*, vol. 21, no. 9, pp. 1167–1178, 2002.
7. A. Kelemen, G. Szkely, and G. Gerig, "Elastic model-based segmentation of 3-d neuroradiological data sets," *IEEE Transactions on Medical Imaging*, vol. 18, no. 10, pp. 828–839, 1999.

8. D. Rückert, A. F. Frangi, and J. A. Schnabel, "Automatic construction of 3-d statistical deformation models of the brain using nonrigid registration," *IEEE Transactions on Medical Imaging*, vol. 22, no. 8, pp. 1014–1025, 2003.
9. A. F. Frangi, D. Rueckert, J. A. Schnabel, and W. J. Niessen, "Automatic construction of multiple-object three-dimensional statistical shape models: Application to cardiac modeling," *IEEE Transactions on Medical Imaging*, vol. 21, no. 9, pp. 1151–1166, 2002.
10. R. Chandrashekara, A. Rao, G. I. Sanchez-Ortiz, R. H. Mohiaddin, and D. Rückert, "Construction of a statistical model for cardiac motion analysis using nonrigid image registration," in *Information Processing in Medical Imaging*, ser. Lecture Notes in Computer Science, C. Taylor and J. A. Noble, Eds., vol. 2732. Berlin: Springer Verlag, 2003, pp. 599–610.
11. J. Lötjönen, S. Kivistö, J. Koikkalainen, D. Smutek, and K. Lauerma, "Statistical shape model of atria, ventricles and epicardium from short- and long-axis mr images," *Medical Image Analysis*, vol. 8, pp. 371–386, 2004.
12. P. Yushkevic, P. T. Fletcher, S. Joshi, A. Thall, and S. M. Pizer, "Continuous medial representations for geometric object modeling in 2d and 3d," *Image and Vision Computing*, vol. 21, no. 1, pp. 17–27, 2003.
13. S. Ordas, L. Boisrobert, M. Bossa, M. Laucelli, M. Huguet, S. Olmos, and A. Frangi, "Grid-enabled automatic construction of a two-chamber cardiac PDM from a large database of dynamic 3D shapes," in *IEEE International Symposium of Biomedical Imaging*, 2004, pp. 416–419.
14. T. Takagi and M. Sugeno, "Fuzzy identification of systems and its applications to modeling and control," *IEEE Transactions of Systems, Man and Cybernetics*, vol. 15, no. 1, pp. 116–132, 1985.
15. T. F. Cootes, D. Cooper, C. J. Taylor, and J. Graham, "A trainable method of parametric shape description," *Image and Vision Computing*, vol. 10, no. 5, pp. 289–294, 1992.
16. T. F. Cootes and C. J. Taylor, "Statistical models of appearance for computer vision," Imaging Science and Biomedical Engineering, University of Manchester, Manchester M13 9PT, U.K., http://www.isbe.man.ac.uk/∼bim/Models/app_models.pdf, Tech. Rep., March 2004.
17. J. Gower, "Generalized procrustes analysis," *Psychometrika*, vol. 40, pp. 33–50, 1975.
18. P. J. Besl and N. D. McKay, "A method for registration of 3-d shapes," *IEEE Transaction on Pattern Analysis and Machine Intelligence*, vol. 14, no. 2, pp. 239–256, 1992.
19. R. R. Paulsen and K. B. Hilger, "Shape modeling using markov random field restoration of point correspondences," in *Information Processing in Medical Imaging*, ser. Lecture Notes in Computer Science, C. Taylor and J. A. Noble, Eds., vol. 2732. Berlin: Springer Verlag, 2003, pp. 1–12.
20. J. C. Bezdek, *Pattern Recognition with Fuzzy Objective Function Algorithms.* New York: Plenum press, 1981.
21. S. Ordas, H. C. van Assen, B. P. F. Lelieveldt, and A. F. Frangi, "Segmentation performance assessment of an autolandmarked statistical shape model," *submitted.*